Available online at www.sciencedirect.com

ScienceDirect

journal homepage: http://www.elsevier.com/locate/rpor

Set-up error validation with EPID images: Measurements vs Egs_cbct simulation

D. van Eeden, F.H.J. O'Reilly, F.C.P. du Plessis*

Medical Physics Department, Faculty of Health Sciences, University of the Free State, P.O. Box 339, Bloemfontein, 9300 South Africa

ARTICLE INFO

Article history:
Received 2 May 2019
Accepted 21 September 2019
Available online 21 October 2019

Keywords:
Cone-beam CT
EPID
Image acquisition interval
Monte Carlo
egs_cbct

ABSTRACT

Aim: In this study, the egs_cbct code's ability to replicate an electronic portal imaging device (EPID) is explored.

Background: We have investigated head and neck (H&N) setup verification on an Elekta Precise linear accelerator. It is equipped with an electronic portal imaging device (EPID) that can capture a set of projection images over different gantry angles.

Methods and materials: Cone-beam computed tomography (CBCT) images were reconstructed from projection images of two different setup scenarios. Projections of an Anthropomorphic Rando head phantom were also simulated by using the egs_cbct Monte Carlo code for comparison with the measured projections.

Afterwards, CBCT images were reconstructed from this data. Image quality was evaluated against a metric defined as the image acquisition interval (IAI). It determines the number of projection images to be used for CBCT image reconstruction.

Results: From this results it was established that phantom shifts could be determined within 2 mm and rotations within one degree accuracy using only 20 projection images (IAI = 10 degrees). Similar results were obtained with the simulated data.

Conclusion: In this study it is demonstrated that a head and neck setup can be verified using substantially fewer projection images. Bony landmarks and air cavities could still be observed in the reconstructed Rando head phantom. The egs_cbct code can be used as a tool to investigate setup errors without tedious measurements with an EPID system.

1. Introduction

Patient positioning accuracy can be verified from EPID images before radiation treatment takes place. For example, a set of EPID projection images can be obtained and transversal CBCT slices of the patient can then be reconstructed to obtain a set of transversal images for the patient that includes the treatment volume. Corresponding reference images obtained through a CT scan of the patient can then be superimposed on them to verify the patient setup. Usually, bony landmarks act as reference points for image overlay evaluation. Instead of bony landmarks, fiducial markers can also be used inside the patient to act as image matching points. The shift and rotation of the patient are recorded through matching software of the system.

Monte Carlo simulation of radiation transport has led to sophisticated patient dose calculation with numerous examples of dose calculation engines such as the EGSnrc based DOSXYZnrc, Penelope, GEANT, and other codes.[1–3] Recently, the EGSnrc_cbct code has been developed to simulate CT

* *Corresponding author.*
E-mail address: vaneedend@ufs.ac.za (D. van Eeden).

https://doi.org/10.1016/j.rpor.2019.09.013

Fig. 1 – The Rando head phantom, the phantom setup is assisted using the green lasers.

scanners that produce transmission data, enabling image reconstruction from filtered back projections. It was written in C++ by Ernesto Mainegra-Hing and Iwan Kawrakow.[4,5] It can be used to set up a CBCT imaging system and has proved to be successful in previous studies. The egs_cbct code has been used for scatter estimations in a chest phantom,[6] an Elekta XVI CBCT imaging system[7] and an onboard imaging panel.[8] In a recent study, the code proved to be successful for the simulation of fan beam CT configuration for Hounsfield unit verification.[9]

In this study, the egs_cbct code's ability to replicate an electronic portal imaging device (EPID) is explored since they are used in image-guided radiation therapy (IGRT) which forms part of modern radiation therapy.[10–14] They can be used to confirm tumour location and to facilitate correct patient set-up prior to radiation treatment, therefore reducing the risk of dose misadministration to the target and surrounding radiosensitive structures.[11–13,15–17] Small treatment margins used for intensity modulated radiation therapy (IMRT) and volumetric modulated arc therapy (VMAT) demand accurate tumour localisation.

Since the radiation beam of the linear accelerator is used as the X-ray source for the EPID, it results in low contrast images.[11] Megavoltage x-ray interactions are dominated by the Compton process in tissue-equivalent materials. The intensity of these interactions is proportional to the relative electron density per unit volume and is similar for soft tissue e.g. muscle and heart tissue. This results in poor soft tissue contrast in megavoltage images and is of the same order as image noise. Substantially lower or higher electron density tissue, such as the lung and bone, will show a better contrast in reconstructed CBCT images.

Several methods have been explored to minimise the dose received by patients during high energy imaging. These methods can include limiting the field of view, limiting the number of projection and using post-processing techniques to improve the image quality.[18] Although it leads to a dose reduction, it also limits the anatomical information in the images. As an alternative, better imaging receptors have been developed by leading vendors such as Varian Medical Systems (Mountain View, CA) and Siemens Medical Solution (Concord, CA). The latter developed a system called MVision with improved detection quantum efficiency and faster read-out time.[19] They reported that an object with 1% electron density contrast could be detected using this system with 10c Gy at the isocentre.[20] Slightly higher doses of 16 cGy were obtained by Varian Medical Systems (Mountain View, CA) with an image receptor consisting of a thallium-doped caesium iodide [CsI(TI] scintillator where doses of 0.023 cGy can be used to form projection images.[21]

Our study involved using the egs_cbct Monte Carlo code to model an EPID imaging system for an Elekta Precise linear accelerator (Elekta Oncology Systems, Crawley, UK). A series of scenarios were devised to assess the accuracy of the egs_cbct code in depicting setup errors in simulated EPID images. The possibility of reducing the number of EPID images of a Rando

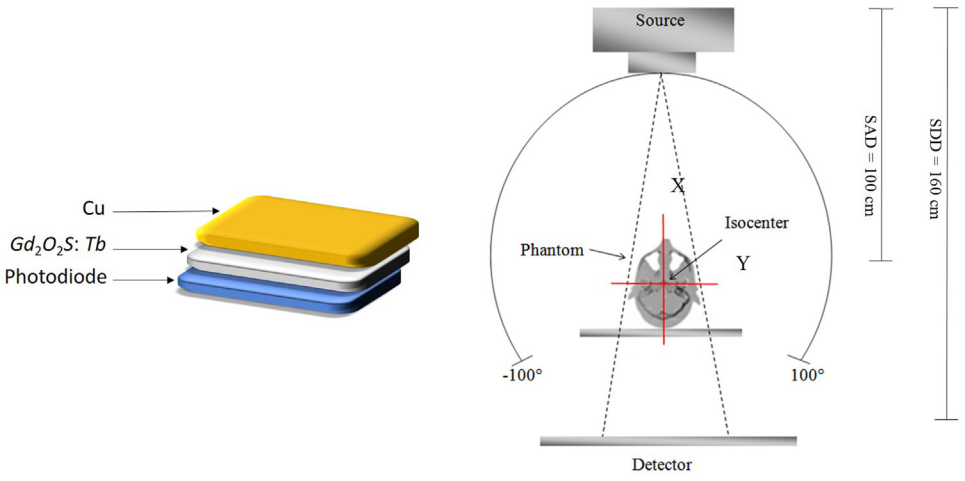

Fig. 2 – a) The terbium doped gadolinium oxysulfide (Gd_2O_2S: Tb) sandwiched between a sheet of Cu and an array of photodiodes. b) The setup used for the simulation of the projection images in egs_cbct.

Head-and-Neck phantom, to reduce the dose, was investigated.

2. Methods and materials

The radiation dose is a dominant factor when EPID imaging is used to locate and confirm tumour positions. It can be reduced when the number of projection images necessary to determine patient shift and rotation is minimized. We introduce a parameter called image acquisition interval (IAI) to study patient shift and rotation accuracy when the number of projection images are reduced but at equally spaced angles. It is the arc interval (in degrees) at which EPID transmission images are sampled for CBCT image reconstruction. Sets of EPID images were obtained from measurements and simulations and reconstructed for different IAI values. The resulting transversal image quality was determined with the contrast-to-noise ratio (CNR) and the signal-to-noise ratio (SNR). The shift and rotation setup errors were calculated on these images by comparing the original images for those obtained for a shifted and rotated phantom. It was compared for increasing IAI values to investigate how fewer projection images could still be used to detect these shifts and rotations.

The egs_cbct Monte Carlo code was used to simulate the above measured data for the purpose of benchmarking it for EPID studies. Reconstructed transversal images from the CBCT simulations were also obtained with increasing IAI. CNR, SNR, and phantom shift and rotation was investigated as in the measured cases.

2.1. *Image acquisition*

2.1.1. *Measurements*

A Rando head phantom (Rando phantom, The Phantom Laboratory, Salem, NY) was set up at the isocenter of an Elekta Precise linear accelerator. This phantom is shown in Fig. 1. The iViewGT EPID requires typically two to four monitor units (MUs) for a 16-bit portal image. This system provides 2D MV planar images within a fraction of a second, making on-line patient position correction possible.[22]

EPID projection images were acquired at one degree gantry angle intervals from -100° to 100°. For each image, one monitor unit of radiation was used for a 6 MV x-ray beam. The radiation field size was $25 \times 25\,cm^2$ at the isocenter, corresponding to $40 \times 40\,cm^2$ at the EPID surface. The EPID registered images in a 1024×1024 matrix with a pixel size of 0.025 cm at the isocenter. The source-to-EPID distance (SDD) is fixed at 160 cm. The 200 images were used as the basis for CBCT image reconstruction from which images were sampled as a function of IAI.

2.1.2. *Simulation*

The ctcreate[23] program was used to convert the CT images of the phantom into a format consisting of the material and density information needed for the egs_cbct simulations. Transmission images of the phantom model were obtained from radiation transport simulations through the phantom model. The energy spectrum of a previously obtained Elekta Precise source model was used as an input x-ray source. The simulated detector material, SSD, SAD and the voxel size of the detector corresponded to that of the Elekta Precise EPID configuration. The a-Si flat panel imager (EPID) used in this study was the iViewGT from Elekta. A typical EPID relies on an indirect photon detection mechanism. The scintillation material, terbium doped gadolinium oxysulfide (Gd_2O_2S: Tb), is sandwiched between a metal sheet top layer of 1 mm copper and a pixelated array of photodiodes typically referred to as an active matrix flat panel imager (AMFPI).[24–26] The detector and the setup used for the egs_cbct simulation is shown in Fig. 2 below.

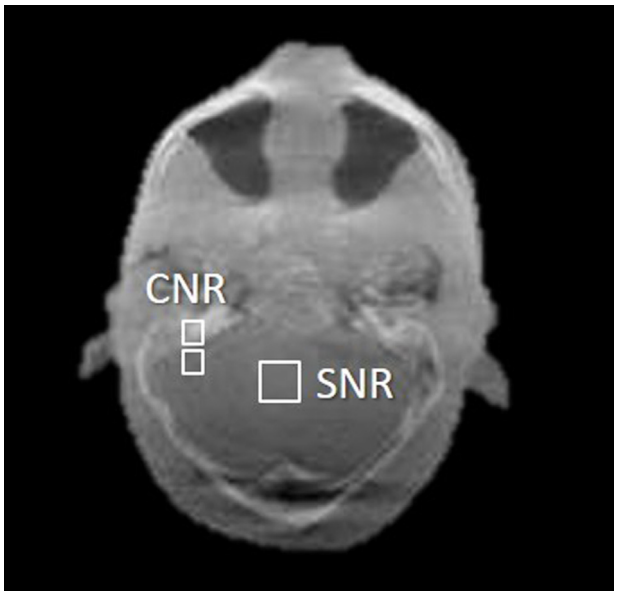

Fig. 3 – Positions of the ROIs for the calculation of the SNR and the CNR.

Simulated data were obtained over the same arc length as during measurements. The transport conditions set prior to simulation included energy cut-offs of 0.010 and 0.7 MeV for photons and electrons, respectively. Atomic relaxations, Rayleigh scattering and bound Compton scattering were not requested. Spin effects were implemented and the electron-step algorithm and boundary cross algorithm (BCA) was PRESTA-II and PRESTA-I, respectively. The skin depth for the BCA was set to three elastic mean free paths.

2.2. *Image reconstruction*

CBCT images were reconstructed from EPID images acquired over a 200 degree arc length. The chosen slice thickness was 1.6 mm and the reconstruction image matrix size was 256×256. In each EPID image, row profiles, corresponding to a specific z-position along the phantom. Before reconstruction, each measured EPID image was corrected for (I) detector offset, (II) detector rotation and, (III) gantry angle variation. The gantry angle read-out on the Elekta accelerator desktop was used as the reference and confirmed by independent gyrometer measurements.

Six sets of transmission images were sampled from the measured and simulated data for image reconstruction. Each

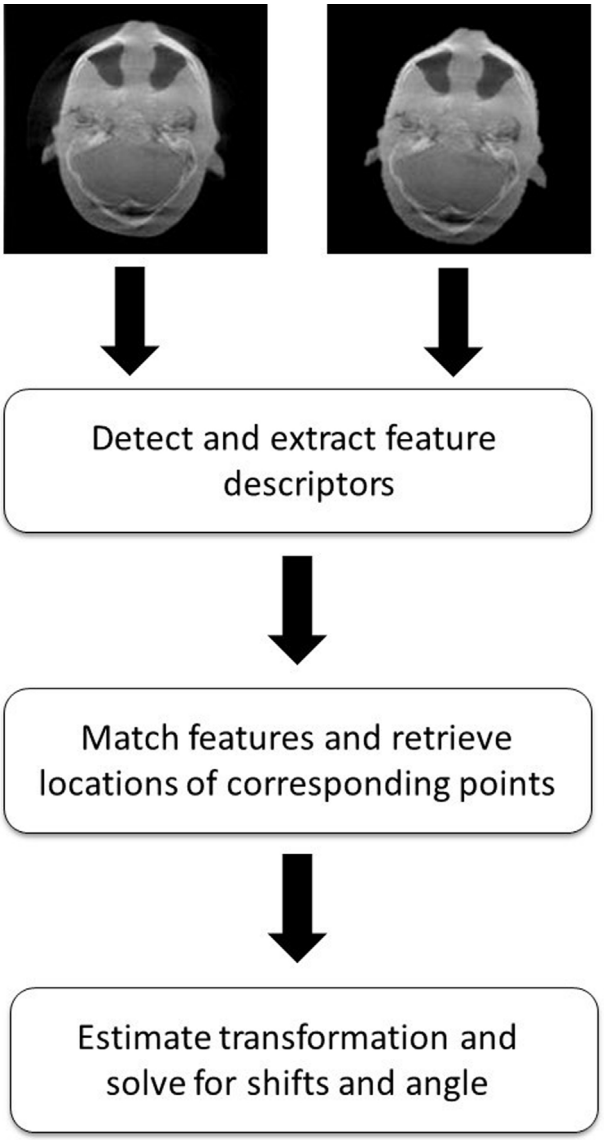

Fig. 4 – The schematic of the method used in MATLAB to determine the shifts and angle difference between two images.

set had a unique IAI value namely 1, 2, 3, 4, 5, 6, 7, 8, 9, and 10 degrees respectfully.

The Interactive Data Language (IDL) software package[27] was used to develop tools for the reconstruction of CBCT (transversal) images from the set of measured EPID transmission images obtained above. A Feldkamp-type filtered backprojection (FBP) algorithm[28,29] was used for CBCT image reconstruction using the geometry-corrected EPID images.

The simulated EPID images were used to reconstruct transversal images with the Open Source Cone-beam Reconstructor (OSCaR) software from the American Association of Physicists in Medicine (AAPM).[30] This software uses the Feldkamp-Davis-Kress (FDK) algorithm and suitable reconstruction filters.

There are high-pass filters and low-pass filters that can be used for the filtering of the projection data. The Ram-Lak filter is a high-pass filter and will sharpen parts of the image where there is a sudden change in signal, e.g. at the edges. This filter will unfortunately amplify statistical noise and can be used in combination with a low-pass filter.[31] These combination filters decrease the image resolution and; therefore, the ramp filter was used for all the images in this study.

2.3. *Image quality*

From each set of reconstructed transversal images obtained from measured and simulated data, the signal-to-noise (SNR) and contrast-to-noise (CNR) ratios were calculated. For the SNR a region-of-interest (ROI) was drawn in on a uniform part of the reconstructed transversal image slice under consideration as seen in Fig. 3 below. From the same image, the CNR was calculated from pixel values in two ROIs, shown as the smaller squares, each of which is assumed to have a uniform, but different pixel value. One ROI was drawn in on a bony landmark and one adjacent to that representing background. A bony landmark was chosen for contrast calculation since it is used most frequently to detect patient displacement and rotation during setup verification.

The level of noise in the reconstructed image is determined by:

$$SNR = \bar{mean}/\bar{\sigma} \quad (1)$$

where $\bar{mean}$ represents the mean pixel value and $\bar{\sigma}$ the standard deviation in the ROI.

The CNR calculates the mean and standard deviation of the pixel values of an object and the homogenous background surrounding the object.[20,32]

$$CNR = |S - S_{BG}|/\sigma \quad (2)$$

where S and S_{BG} are the mean pixel values in the insert and background region, respectively, and σ is the average standard deviation of the pixel value in the insert and the background.

The above method was repeated for images reconstructed using increasing IAI values.

2.4. *Phantom positional accuracy and rotation detection*

In this study bony anatomical points were chosen in the Rando head phantom to study shift and rotation detection.

The head phantom was imaged for two cases with the EPID system to detect positional and rotational indifferences between consecutive setups. In the first case, the phantom was imaged as described in section 2.1.1 to obtain reference data. In the second case, the head phantom was moved a known distance (2 cm) first in a lateral direction and then rotated by five degrees. 200 planar EPID images were taken for CBCT data reconstruction. The matching transversal slice images of these two cases were compared with the reference data to determine the shifts and rotation.

A MATLAB code was used to determine the shifts and rotations between the images. The Speeded-up Robust

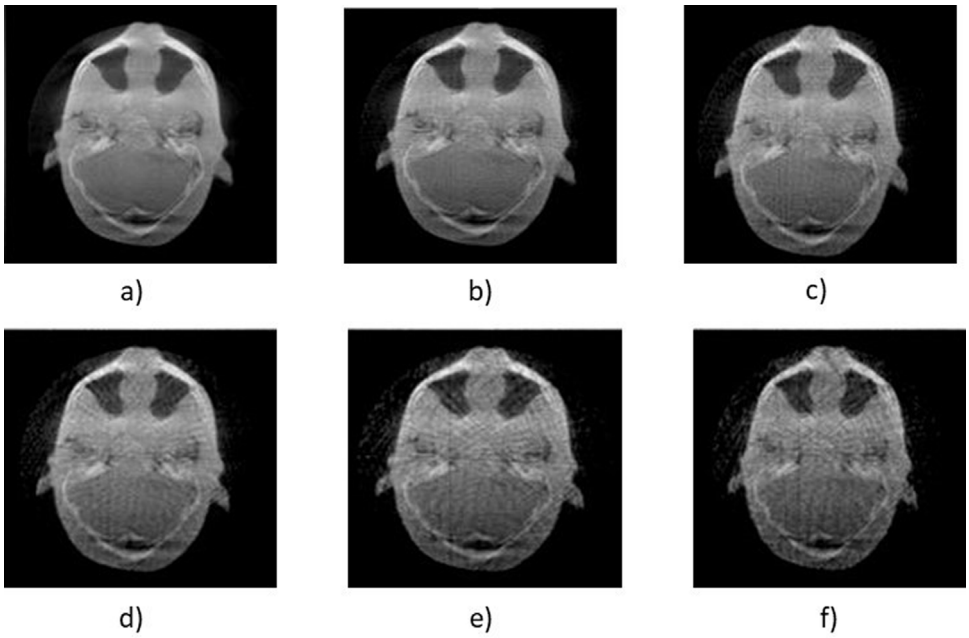

Fig. 5 – Reconstructed images of the Rando head phantom over 200° arc length for IAI of (a) 1°, (b) 2°, (c) 3°, (d) 4°, (e) 5° and (f) 6°.

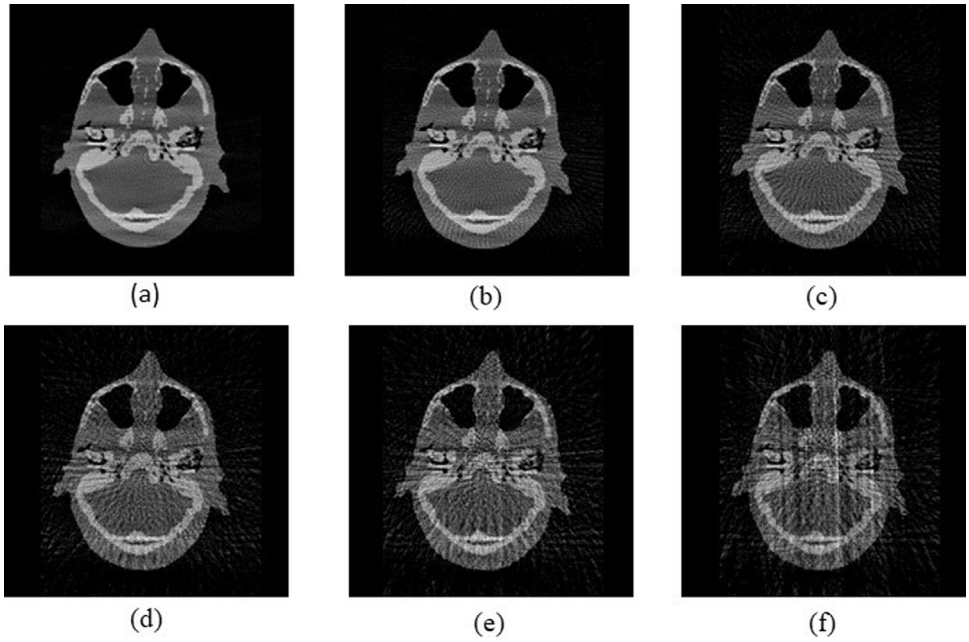

Fig. 6 – Reconstructed images of the simulated Rando head phantom over 200° arc length for IAI of (a) 1°, (b) 2°, (c) 3°, (d) 4°, (e) 5° and (f) 6°.

Features (SURF) algorithm was used to find the corresponding points between two images that are rotated with respect to each other.[33] The process can be seen below in Fig. 4.

This process was repeated for the simulated egs_cbct data to compare phantom displacement and rotation assessment with the measured data.

3. Results

3.1. *Image reconstruction*

Image acquisition-, patient dose-, and reconstruction time can be reduced by using fewer projection images. In

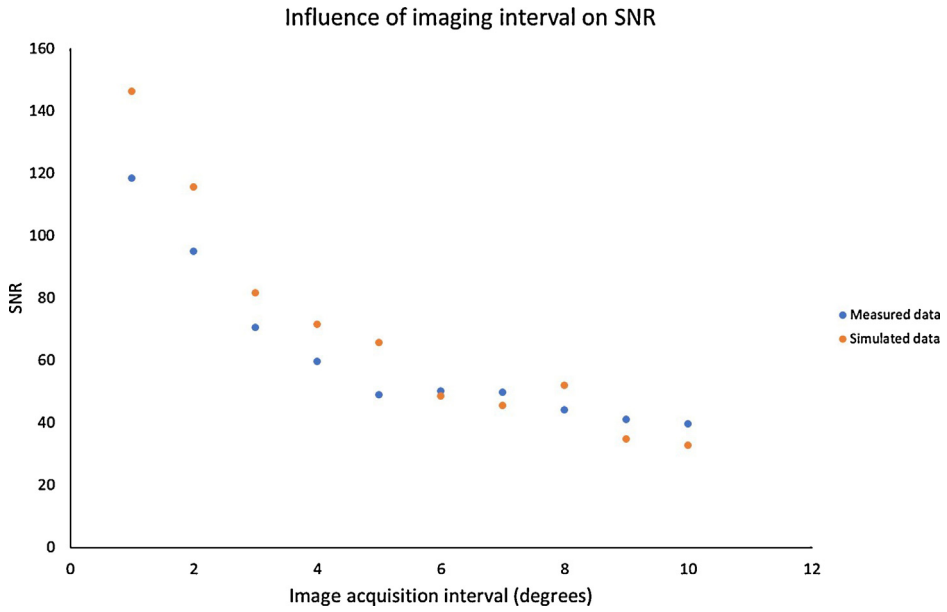

Fig. 7 – SNR as a function of IAI. It was obtained from CBCT images reconstructed from planar images sampled at increasing IAI.

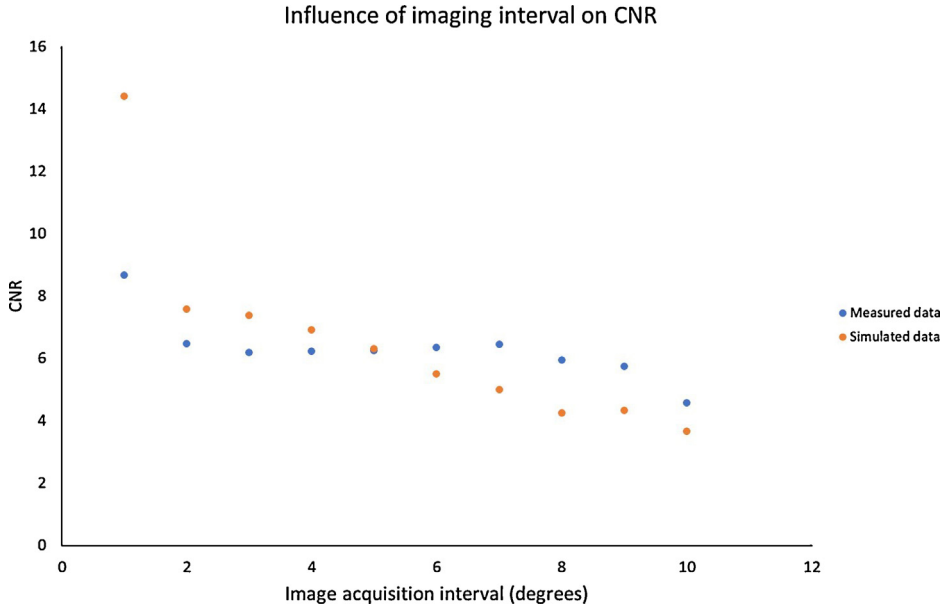

Fig. 8 – CNR as a function of IAI, obtained from CBCT images reconstructed from planar images sampled at increasing IAI.

this study the IAI was used to determine the number of projection images. However, there exists a trade-off between image quality and the IAI as seen in Fig. 5. Visually, the image (panel f) do look degraded at an IAI = 6 degrees. Similar results were obtained from the images reconstructed from egs_cbct EPID simulations as seen in Fig. 6.

In Fig. 6, egs_cbct simulated EPID images were used to reconstruct the images using the OSCaR reconstruction algorithm.

3.2. *Image quality*

The SNR and CNR were calculated for the reconstructed transversal images (see e.g. Figs. 7 and 8) at increasing IAI values. As it increases, the reconstructed transversal image noise increased causing both the SNR and CNR to deteriorate. This is seen in Figs. 7 and 8.

In the next section, we investigated the accuracy with which we could measure patient shift and rotation as an increasing function of IAI.

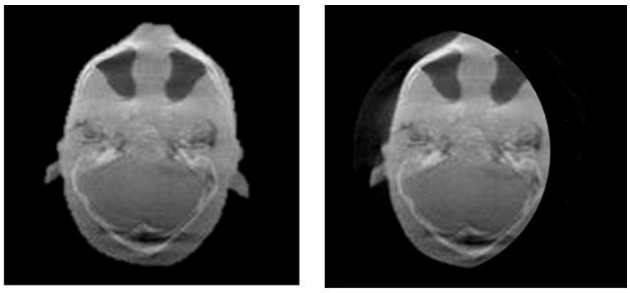

Fig. 9 – Reconstructed data for a Rando phantom. The phantom was shifted 2.0 cm lateral in panel (b).

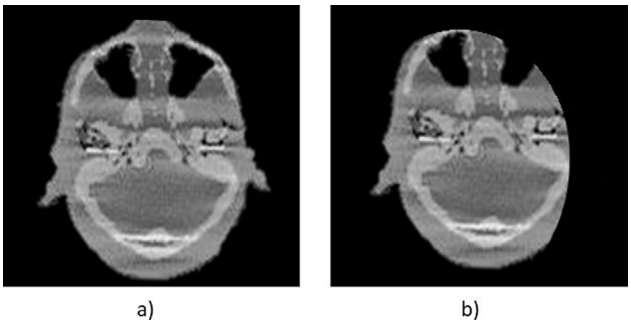

Fig. 10 – Reconstructed data for the simulated Rando phantom. The phantom was shifted 2.0 cm lateral in panel (b).

3.3. *Phantom positional accuracy and rotation*

In Fig. 9 the reconstructed transverse images are shown with (a), the Rando head phantom set up at isocenter, and (b), the phantom in the same position but the treatment couch moved a known distance of 2.0 cm in the lateral direction. The corresponding simulations can be seen in Fig. 10.

From these images, the calculated shift was determined by determining the distance between the corresponding points obtained in MATLAB (Fig. 4). In the next step, the IAI was increased to determine a new set of projection images to reconstruct the transversal images in the same z-plane as that shown in Figs. 9 and 10. Again, the calculated shift was determined from the same corresponding points on the images. Differences between the calculated and known shift as a function of IAI are shown in Fig. 11.

As seen below in Figs. 12 bony landmarks were used to determine the positional shift and rotation between the two datasets. The landmarks were identified by the MATLAB code as described in Fig. 4.

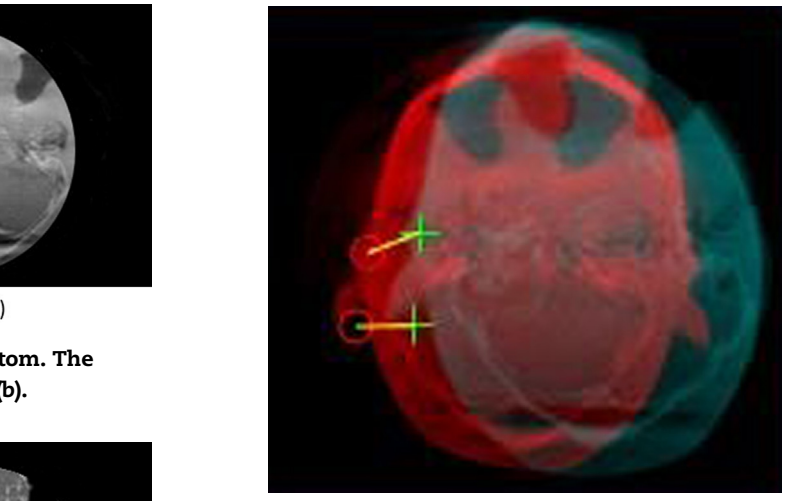

Fig. 12 – The corresponding points used to determine the rotation between the two images.

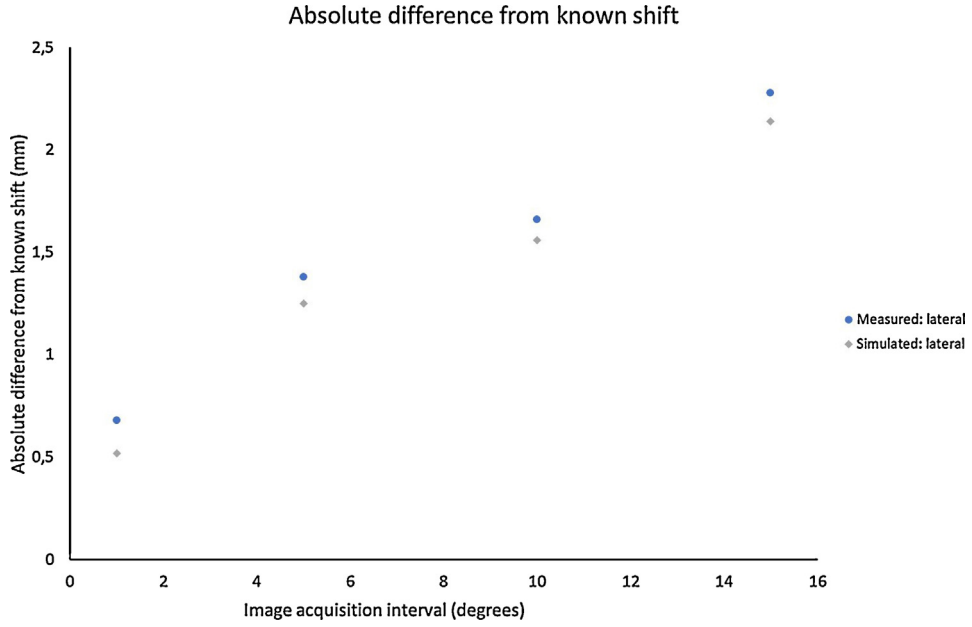

Fig. 11 – Difference between calculated and known shifts for data points between the images in Figs. 9 and 10 for increasing IAI. Lateral shift differences were calculated for the measured and the simulated data.

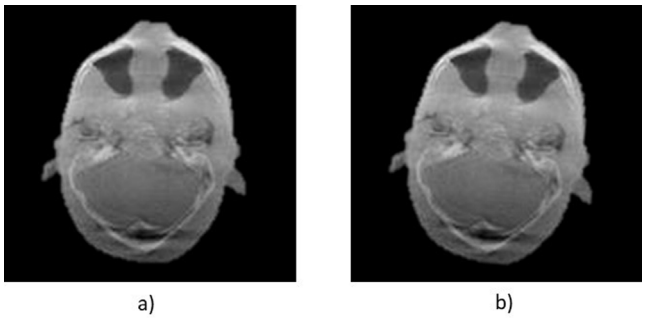

Fig. 13 – Reconstructed data for a Rando head phantom. The phantom was tilted five degrees clockwise in panel.

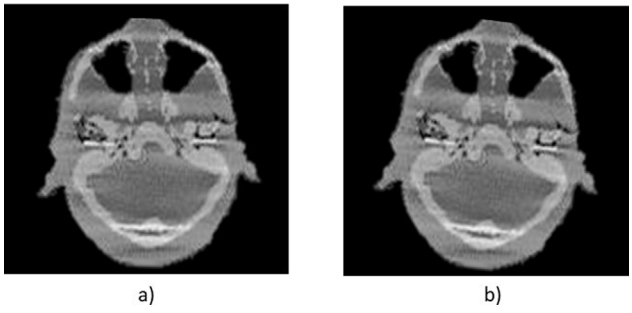

Fig. 14 – Reconstructed data for the simulated Rando head phantom. The phantom was tilted five degrees clockwise.

The following images were used to determine the rotation between the measured and simulated data sets. Each of these datasets is acquired with a IAI of 1 (Figs. 13–14).

New sets of transversal images were constructed for IAI values of 1°, 5°, 10° and 15°. The difference between the calculated and known rotations for increasing IAI is shown in Fig. 15.

It is seen here that the accuracy of the calculation for rotation is dependent on the IAI. To be accurate within one degree of rotation, the IAI should not be larger than 8 degrees.

4. Discussion

For the measured data, the CNR stays relatively constant for IAI values greater than 5 degrees. The SNR reaches 50% at IAI = 4 degrees and 30% at IAI = 10 degrees. From this information, it seems that a further increase in IAI would not affect CNR and SNR significantly for IAI ≥ 10 degrees. Similar results are seen for the simulated data.

As expected, an increase in the IAI would degrade the SNR and CNR in the reconstructed images as can be seen in Figs. 5 and 6. At the same time, differences between the calculated and known shifts in general become larger as seen in Fig. 11. To keep the calculated shift inaccuracy within 2 mm, the IAI must be limited to 10 degrees which is confirmed by the data from egs_cbct simulation results. Shift inaccuracies larger than 2 mm would become clinically relevant and they occur at IAI values larger than 10 degrees. If an IAI value of 10 degrees is used, it can reduce the planar image acquisition and CBCT reconstruction time by a factor of 10. When patient shift and rotation detection is the prime objective of imaging, image quality is not an important factor since high contrast landmarks can be identified to detect a patient shift during setup.

Fewer reconstruction images are advantageous to reduce reconstruction time and dose to the patient during image acquisition. In this study, bony structures found in the head and neck can be used effectively to detect phantom shift and

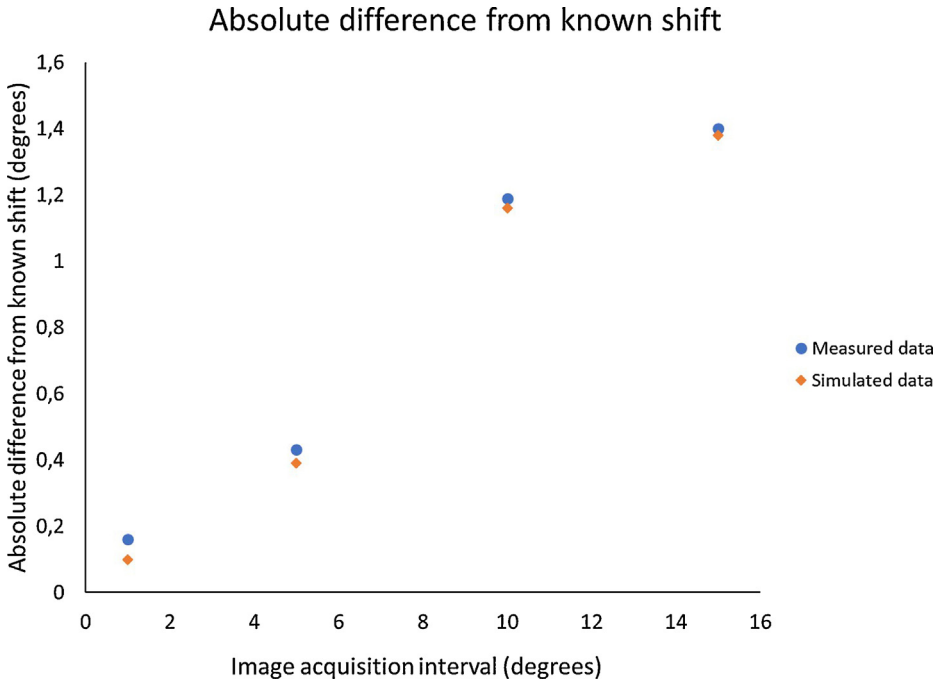

Fig. 15 – The difference between the calculated and known rotation calculated for images reconstructed for IAI values of 1°, 5°, 10° and 15°.

rotation up to an IAI value of 8 degrees. The method developed in this study specifically focussed on head and neck setup verification and may not be applicable for other treatment sites in the body.

The egs_cbct code is useful to investigate the characteristics of an EPID system. Good correlation was obtained for the measured and simulated SNR, CNR, shift and rotation measurements. The most powerful of these applications is that egs_cbct can be used to evaluate a priori if a given EPID system can be used with minimal dose to the patient in its ability to verify patient shifts with a maximum IAI to decrease the amount of EPID images needed for image reconstruction. The egs_cbct simulations verified the concept of IAI used to reduce patient dose without distorting patient shift and rotation detection accuracy to clinically significant values.

5. Conclusion

Head and neck setup error accuracy as a function of IAI was investigated. An Elekta Precise linac (6 MV beam) equipped with an on-board EPID was investigated. This EPID was used to obtain a set of projection images for reconstruction of megavoltage CBCT image data sets. Projections images were simulated with the egs_cbct code to verify the setup errors found with the measured data.

The SNR and CNR values were calculated on the Rando head phantom for the measured and simulated data. Both these values decreased as the IAI increased but tended to stabilise at IAI larger than 5 degrees. The SNR decreased by 60 percent and the CNR decreased by 25 percent for IAI between 1 and 5 degrees.

Positional accuracy was verified through measurements of simulated shifts and rotations of the Rando head phantom. This was repeated for reconstructed images using various IAIs. The absolute difference from known shifts (all directions) and rotation was less than 1 mm and 1° for 200 projection images and less than 2 mm and 1° for 20 projection images. For image acquisition over 200 degrees, a maximum IAI of 10 degrees is recommended.

In this study it is demonstrated that head and neck setup can be verified using substantially fewer projection images over a gantry arc of 200 degrees. Since image contrast is low in megavoltage images, bony landmarks still appear well defined despite fewer projection images. This enables head and neck setup accuracy within 2 mm and one degree using only 20 projection images (IAI = 10 degrees). The egs_cbct code can be used as a tool to investigate setup errors without tedious measurements with an EPID system. This study can be extended to other anatomical regions and more complex errors.

Financial disclosure

This research project was funded by the South African Medical Research Council with funds from National Treasury under its Economic Competitiveness and Support Package in terms of the MRC's Flagships Awards Project SAMRC-RFA-UFSP-01-2013/HARD.

Conflict of interest

None declared.

REFERENCES

1. Chow JCL, Jiang R, Owrangi AM. Dosimetry of small bone joint calculated by the analytical anisotropic algorithm: a Monte Carlo evaluation using the EGSnrc. *J Appl Clin Med Phys* 2013;**15**(January 6 (1)):262–73.
2. Faddegon BA, Kawrakow I, Kubyshin Y, Perl J, Sempau J, Urban L. Accuracy of EGSnrc, Geant4 and PENELOPE Monte Carlo systems for simulation of electron scatter in external beam radiotherapy. *Phys Med Biol* 2009;**54**(October 21 (20)):6151–63.
3. Archambault JP, Mainegra-Hing E. Comparison between EGSnrc, Geant4, MCNP5 and Penelope for mono-energetic electron beams. *Phys Med Biol* 2015;**60**(13):4951.
4. Mainegra-Hing E, Kawrakow I. Variance reduction techniques for fast Monte Carlo CBCT scatter correction calculations. *Phys Med Biol* 2010;**55**(August 21 (16)):4495–507.
5. Mainegra-Hing E, Kawrakow I. Fast Monte Carlo calculation of scatter corrections for CBCT images. *J Phys: Conf Ser* 2008;**102**(1):012017.
6. Thing RS, Mainegra-Hing E. Optimizing cone beam CT scatter estimation in egs_cbct for a clinical and virtual chest phantom. *Med Phys* 2014;**41**(July 1 (7)):071902.
7. Thing RS, Bernchou U, Mainegra-Hing E, Brink C. Patient-specific scatter correction in clinical cone beam computed tomography imaging made possible by the combination of Monte Carlo simulations and a ray tracing algorithm. *Acta Oncol* 2013;**52**(October 1 (7)):1477–83.
8. Chang J, Zhou L, Wang S, Clifford Chao KS. Panoramic cone beam computed tomography. *Med Phys* 2012;**39**(May 1 (5)):2930–46.
9. van Eeden D, du Plessis F. EGS_cbct: Simulation of a fan beam CT and RMI phantom for measured HU verification. *Phys Med: Eur J Med Phys* 2016;**32**(October 1 (10)):1375–80.
10. Development of a QA phantom and automated analysis tool for geometric quality assurance of on-board MV and kV x-ray imaging systems - Mao- 2008 - Medical Physics - Wiley Online Library [Internet]. [cited 2019 Apr 5]. Available from: https://aapm.onlinelibrary.wiley.com/doi/abs/10.1118/1.2885719.
11. Cho Y, Moseley DJ, Siewerdsen JH, Jaffray DA. Accurate technique for complete geometric calibration of cone-beam computed tomography systems. *Med Phys* 2005;**32**(4):968–83.
12. Gayou O. Influence of acquisition parameters on MV-CBCT image quality. *J Appl Clin Med Phys* 2012;**13**(1):14–26.
13. Ford JC, Zheng D, Williamson JF. Estimation of CT cone-beam geometry using a novel method insensitive to phantom fabrication inaccuracy: Implications for isocenter localization accuracy. *Med Phys* 2011;**38**(6Part1):2829–40.
14. Robert N, Watt KN, Wang X, Mainprize JG. The geometric calibration of cone–beam systems with arbitrary geometry. *Phys Med Biol* 2009;**54**(November (24)):7239–61.
15. Developments in megavoltage cone beam CT with an amorphous silicon EPID: Reduction of exposure and synchronization with respiratory gating - Sillanpaa- 2005 - Medical Physics - Wiley Online Library [Internet]. [cited 2019 Apr 5]. Available from: https://aapm.onlinelibrary.wiley.com/doi/abs/10.1118/1.1861522.
16. Current concepts on imaging in radiotherapy | SpringerLink [Internet]. [cited 2019 Apr 5]. Available from: https://link.springer.com/article/10.1007/s00259-007-0631-y.

17. A comparison of kilovoltage and megavoltage cone beam CT in radiotherapy | Journal of Radiotherapy in Practice | Cambridge Core [Internet]. [cited 2019 Apr 5]. Available from: https://www.cambridge.org/core/journals/journal-of-radiotherapy-in-practice/article/comparison-of-kilovoltage-and-megavoltage-cone-beam-ct-in-radiotherapy/F76ACAB0E85D63FF87D4480CD704FB09.
18. Loose S, Leszczynski KW. On few-view tomographic reconstruction with megavoltage photon beams. *Med Phys* 2001;**28**(August 1 (8)):1679–88.
19. Pouliot J, Bani-Hashemi A, Chen J, Svatos M, Ghelmansarai F, Mitschke M, et al. Low-dose megavoltage cone-beam CT for radiation therapy. *Int J Radiat Oncol Biol Phys* 2005;**61**(February 1 (2)):552–60.
20. Gayou O, Miften M. Commissioning and clinical implementation of a mega-voltage cone beam CT system for treatment localization. *Med Phys* 2007;**34**(August (8)):3183–92.
21. Seppi EJ, Munro P, Johnsen SW, Shapiro EG, Tognina C, Jones D, et al. Megavoltage cone-beam computed tomography using a high-efficiency image receptor. *Int J Radiat Oncol Biol Phys* 2003;**55**(March 1 (3)):793–803.
22. Team EW. iViewGTTM [Internet]. Elekta AB. [cited 2018 Nov 13]. Available from: https://www.elekta.com/radiotherapy/treatment-solutions/imaging/iviewgt.html#iview-gt-ar.
23. Ma C.M., Rogers D.W.O., Walters B.R.B. DOSXYZnrc users manual [Internet]. Ottawa: National Research Council of Canada; 2010 Jan [cited 2017 Jan 4]. Report No.: NRCC Report PIRS-794revB. Available from: https://www.researchgate.net/publication/44064801_DOSXYZnrc_users_manual.
24. Street R.A., Nelson S., Antonuk L., Mendez V.P. Amorphous Silicon Sensor Arrays for Radiation Imaging. MRS Online Proceedings Library Archive [Internet]. 1990 ed[cited 2018 Nov 13];192. Available from: https://www.cambridge.org/core/journals/mrs-online-proceedings-library-archive/article/amorphous-silicon-sensor-arrays-for-radiation-imaging/90E3BE0A5FA3F57C793B90E599C6AE04.
25. Antonuk LE, Yorkston J, Boudry J, Longo MJ, Jimenez J, Street RA. Development of hydrogenated amorphous silicon sensors for high energy photon radiotherapy imaging. *IEEE Trans Nucl Sci* 1990;**37**(April (2)):165–70.
26. Munro P, Bouius DC. X-ray quantum limited portal imaging using amorphous silicon flat-panel arrays. *Med Phys* 1998;**25**(May (5)):689–702.
27. IDL Software - The Trusted Scientific Programming Language | Harris Geospatial [Internet]. [cited 2017 Oct 17]. Available from: http://www.harrisgeospatial.com/SoftwareandTechnology/IDL.aspx.
28. Feldkamp LA, Davis LC, Kress JW. Practical cone-beam algorithm. *J Opt Soc Am A* 1984;**1**(June 1):612–9.
29. Kak A, Slaney M [cited 2015 Nov 24]. 335 p. (Classics in Applied Mathematics). Available from: http://epubs.siam.org/doi/book/10.1137/1.9780898719277, 2001.
30. Rezvani N, Aruliah D, Jackson K, Moseley D, Siewerdsen J. OSCaR: An open-source cone-beam CT reconstruction tool for imaging research. *Med Phys* 2007;**34**(6).
31. Lyra M, Ploussi A. Filtering in SPECT Image Reconstruction. *Int J Biomed Imaging* 2011;**2011**(June 23):e693795.
32. Gayou O, Parda DS, Johnson M, Miften M. Patient dose and image quality from mega-voltage cone beam computed tomography imaging. *Med Phys* 2007;**34**(February (2)):499–506.
33. Bay H, Tuytelaars T, Van Gool L. SURF: Speeded up robust features. In: Leonardis A, Bischof H, Pinz A, editors. *Computer Vision – ECCV 2006. ECCV 2006. Lecture Notes in Computer Science*, vol. 3951. Berlin, Heidelberg: Springer; 2006.